Spaceborne ISAL Imaging Algorithm for High-Speed Moving Targets

Hongfei Yin, Yachao Li, *Member, IEEE*, Liang Guo, *Member, IEEE*, Songyuan Li, *Graduate Student Member, IEEE*, Xuan Wang, *Graduate Student Member, IEEE*, Liang Han, and Mengdao Xing, *Fellow, IEEE*

***Abstract*—During the spaceborne inverse synthetic aperture ladar (ISAL) imaging, the radial velocity between the piggyback satellite of ladar and the observed satellite is usually relatively large, which will introduce the inner-pulse Doppler that cannot be ignored in the echo. In this case, the traditional "stop-and-go" assumption will no longer hold, and the compressed result along the range direction would be seriously broaden. Therefore, to obtain a well-focused ISAL image, this article proposed a spaceborne ISAL imaging algorithm for high-speed moving targets based on the inner-pulse Doppler compensation and residue video phase (RVP) correction. In the article, the estimate method of the radial velocity, the inner-pulse Doppler compensation method, and the RVP correction method are given. After inner-pulse Doppler compensation, RVP correction and translational motion compensation, the range-compressed result under the "stop-and-go" assumption can be obtained, and the target can then be imaged by the traditional ISAL imaging algorithm. The simulation results demonstrate the effectiveness of the proposed algorithm.**

***Index Terms*—High-speed moving targets, inner-pulse Doppler compensation, inverse synthetic aperture ladar (ISAL), residue video phase (RVP) correction.**

I. Introduction

IN RECENT years, a large number of artificial satellites with detection, identification, jamming, and strike capabilities have been launched into space by many countries. These satellites can become weapons during a war. Therefore, we need to enhance our detection capabilities for space satellites [1], [2], [3], [4], [5]. However, the satellites distribute in large range and operates at high speed. So before accurately identifying and classifying the satellites, the long-range high-resolution imaging of high-speed moving targets is an indispensable key technology.

Inverse synthetic aperture ladar (ISAL) realizes high resolution in the range direction by transmitting large-bandwidth signals, and realizes high resolution in the azimuth direction by using synthetic aperture technology, whose resolution is independent of range. Thus, ISAL can break through the limitation of diffraction limit of traditional optical imaging [6], [7], [8], [9] and obtain a 2-D high-resolution images. Meanwhile, since ISAL is an active imaging technology, it can work all days.

The wavelength of ISAL is about 3–4 orders shorter than the wavelength of inverse synthetic aperture radar (ISAR). Therefore, comparing with ISAR, ISAL can obtain a higher resolution image within a shorter accumulation time. In addition, due to the absence of atmosphere in space, we need not compensate for the impact of atmospheric turbulence on the echo during the spaceborne ISAL imaging.

The traditional ISAL imaging algorithm do not consider the high-speed motion of the target, it generally assume that the target moves slowly and use the "stop-and-go" assumption that the target is stationary during a pulse period and is active between two adjacent pulses to analyze the target echo. However, since the working wavelength of ladar is relatively short, ISAL imaging is sensitive to target motion [10]. If the target moves at a high speed relative to ladar, and causes $v \cdot T_p > \rho_r$ (v is the radial velocity of the target relative to radar, T_p is the pulsewidth, and ρ_r is the resolution along the range direction), the motion of the target during a pulse period cannot be ignored and the "stop-and-go" assumption will no longer hold [11], [12]. In fact, the orbiting satellites usually move very fast, and the imaging resolution of ISAL is high, the high-speed motion of the satellites will make the range-compressed result of scatterers shifted and broadened. Therefore, during spaceborne ISAL imaging, the high-speed motion of the satellites should be analyzed and compensated.

The high-speed motion compensation method has been deeply studied in ISAR imaging area, and it mainly include two categories. One category method directly utilizes time–frequency analysis algorithm to produce range-instantaneous Doppler image [13]. However, due to the limitation of cross-terms in

Manuscript received 9 April 2023; revised 15 June 2023; accepted 1 August 2023. Date of publication 7 August 2023; date of current version 21 August 2023. This work was supported in part by the National Key Research and Development Program of China (the Foundation Strengthening Project) under Grant 2018YFA0701903, in part by the National Major in High Resolution Earth Observation under Grant GFZX0403260313, Grant 11-H37B02-9001-19/22, and Grant 30-H30C01-9004-19/21, in part by the Research Plan Project of National University of Defense Technology under Grant ZK18-01-02, in part by the National Natural Science Foundation of China under Grant 61801345, and in part by the Open Foundation of Laboratory of Pinghu. *(Corresponding authors: Yachao Li; Liang Guo.)*

Hongfei Yin is with the Hangzhou Institute of Technology, Xidian University, Hangzhou 311231, China (e-mail: yinhongfei1212@163.com).

Yachao Li is with the National Laboratory of Radar Signal Processing, Xidian University, Xi'an 710071, China (e-mail: ycli@mail.xidian.edu.cn).

Liang Guo, Songyuan Li, Xuan Wang, and Liang Han are with the School of Optoelectronic Engineering, Xidian University, Xi'an 710071, China (e-mail: lguo@mail.xidian.edu.cn; 1090824652@qq.com; wx@stu.xidian.edu.cn; lhan@xidian.edu.cn).

Mengdao Xing is with the National Laboratory of Radar Signal Processing and the Collaborative Innovation Center of Quantum Information of Shaanxi Province, Xidian University, Xi'an 710071, China (e-mail: xmd@xidian.edu.cn).

Digital Object Identifier 10.1109/JSTARS.2023.3302570

time–frequency analysis algorithm, the resolution of target is usually reduced. The other category method is based on the parameter estimation. Some scholars equate the dechirp received signal to a second-order phase [11], [12], [13], [14], [15], [16], [17] or a higher order phase signal [18], [19], [20], then compensate for second-order and higher order phases of the high-speed moving targets' echo by estimating the radial velocity or the phase coefficient. These algorithms can focus well along the range direction to the high-speed moving target, but during the parameter estimation, they require a large amount of computation. Furthermore, all of these methods did not consider the influence of velocity on azimuth phase, which will affect the focusing effect along the azimuth.

Compared to ISAR, the working wavelength of ISAL is short, therefore, ISAL requires higher accuracy for high-speed motion compensation. To analyze the impact of high-speed target motion on ISAL imaging, some scholars established the accurate signal model of high-speed moving targets, and gave the approximation model and its constraint [10]. Some scholars proposed the high-speed moving target imaging algorithm based on Fractional Fourier Transform (FrFT)-CLEAN [21], but this algorithm requires a large amount of computation and cannot extract weak scatterers, leading to the loss of the imaging details.

For these reasons, an ISAL imaging algorithm for spaceborne high-speed moving targets based on the inner-pulse Doppler compensation and residue video phase (RVP) correction is proposed in this article. First, the signal model of high-speed moving targets is established. By analyzing the signal model, it can be known that the speed of moving targets will affect the envelope of the echo, and introduce the inner-pulse Doppler in the echo. Second, the inner-pulse Doppler compensation method based on the velocity estimation is proposed. And the velocity estimate method and the constraint condition of the velocity estimate error are given. Third, after the inner-pulse Doppler compensation, the accurate function of RVP along the azimuth is derived. Finally, after RVP correction and the translational motion compensation, we can obtain the range-compressed result under the "stop-and-go" assumption, and the target can be imaged by the traditional ISAL imaging algorithm.

The rest of the article is organized as follows. In Section II, the signal model of high-speed moving targets is established, and the influence of target speed on ISAL imaging is analyzed. In Section III, the inner-pulse Doppler compensation, RVP correction, and imaging algorithm are presented. The simulated results are provided in Section IV. Section V is the discussion section. Finally, Section VI concludes this article.

II. Signal Model of High-Speed Moving Targets

Below we establish the high-speed moving signal model of a single scatterer.

Assume that the transmission signal is an LFM (linear frequency modulation) signal

$$s = A \cdot \text{rect}\left(\frac{\hat{t}}{T_p}\right) \exp\left(j2\pi f_c t + j\pi\gamma\hat{t}^2\right) \tag{1}$$

where A represents the amplitude. T_p represents the pulsewidth. $\hat{t}$ represents the fast time. $t = \hat{t} + t_m$ represents the full time. $t_m = m/\text{PRF}$ represents the slow time. m represents the mth transmitted pulse. PRF represents the pulse repetition period. f_c represents the carrier frequency and γ represents the chirp rate.

If the radial velocity of the scatterer relative to ladar is v, the instantaneous range between the scatterer and ladar at $(\hat{t}, t_m)$ can be expressed as

$$R = R_0\left(t_m\right) + v\hat{t} \tag{2}$$

where $R_0(t_m)$ represents the range between the scatterer and ladar at t_m.

Then, the echo can be written as

$$\begin{aligned} s_r = {} & \sigma A \cdot \text{rect}\left(\frac{\hat{t} - 2R/c}{T_p}\right) \\ & \cdot \exp\left(j2\pi f_c\left(t - 2R/c\right) + j\pi\gamma\left(\hat{t} - 2R/c\right)^2\right) \end{aligned} \tag{3}$$

where σ is the attenuation coefficient.

If the reference signal is

$$\begin{aligned} s_{\text{ref}} = {} & \text{rect}\left(\frac{\hat{t} - 2R_{\text{ref}}/c}{T_r}\right) \\ & \cdot \exp\left(j2\pi f_c\left(t - 2R_{\text{ref}}/c\right) + j\pi\gamma\left(\hat{t} - 2R_{\text{ref}}/c\right)^2\right) \end{aligned} \tag{4}$$

where R_{ref} represents the reference range. T_r represents the pulsewidth of s_{ref}, which is longer than T_p.

Then, the dechirp received signal can be written as

$$\begin{aligned} s_d = s_r \cdot s_{ref}^* = {} & \sigma A \cdot \text{rect}\left(\frac{\alpha\hat{t} - 2R_0\left(t_m\right)/c}{T_p}\right) \\ & \cdot \exp\left(-j\frac{4\pi}{\lambda}\left(R_0\left(t_m\right) - R_{\text{ref}}\right)\right) \\ & \cdot \exp\left(j4\pi\frac{\gamma}{c^2}\left(R_0^2\left(t_m\right) - R_{\text{ref}}^2\right)\right) \\ & \cdot \exp\left(-j4\pi\left(\frac{\gamma}{c}\left(R_0\left(t_m\right) - R_{\text{ref}}\right) + \frac{v}{\lambda} - 2\gamma v\frac{R_0\left(t_m\right)}{c^2}\right)\hat{t}\right) \\ & \cdot \exp\left(j4\pi\frac{v}{c}\gamma\left(\frac{v}{c} - 1\right)\hat{t}^2\right) \end{aligned} \tag{5}$$

where $[\,]^*$ represents the conjugate operator. $\alpha = (1 - 2v/c)$ represents the scale factor.

However, the dechirp received signal under the "stop-and-go" assumption is given as follows [6]:

$$\begin{aligned} s_{\text{stop\_go}} = {} & \sigma A \cdot \text{rect}\left(\frac{\hat{t} - 2R_0\left(t_m\right)/c}{T_p}\right) \\ & \cdot \exp\left(-j\frac{4\pi}{\lambda}\left(R_0\left(t_m\right) - R_{\text{ref}}\right)\right) \\ & \cdot \exp\left(-j4\pi\gamma\left(\hat{t} - 2\frac{R_{\text{ref}}}{c}\right)\frac{R_0\left(t_m\right) - R_{\text{ref}}}{c}\right. \\ & \left. + 4\pi\gamma\frac{\left(R_0\left(t_m\right) - R_{\text{ref}}\right)^2}{c^2}\right). \end{aligned} \tag{6}$$

By comparing (5) with (6), we can know that due to the high-speed movement of the target, the scale factor α is added to the envelope of (5), and the first-order and second-order phases are also be added to (5), which will affect the range resolution and make the range-compressed result of scatterers shifted and broadened. This means that the imaging algorithm under the traditional "stop-and-go" assumption cannot be directly used to image high-speed moving targets.

The influence of high speed on ISAL imaging in (5) is further analyzed as follows:

1) The influence of high speed on the echo envelope

Since the envelop is affected by the scale factor α, the fast time $\hat{t}$ in (5) should meet

$$\left(-\frac{T_p}{2}+2\frac{R_0}{c}\right)\Big/\alpha \le \hat{t} \le \left(\frac{T_p}{2}+2\frac{R_0}{c}\right)\Big/\alpha. \tag{7}$$

This indicates that the length of the received signal of high-speed moving target is $\Delta\hat{t}=T_p/\alpha$. When the target is far away from the ladar, i.e., $v>0$, $\Delta\hat{t}>T_p$, the length of received signal envelope is increased. If we take the Fourier transform of (5) along the fast time $\hat{t}$, the range-compressed result in frequency-domain will be smaller than $1/T_p$, and the range resolution is improved. When the target is close to the ladar, i.e., $v<0$, $\Delta\hat{t}<T_p$, the length of received signal envelope is decreased. If we take the Fourier transform of (5) along the fast time $\hat{t}$, the range-compressed result in frequency-domain will be greater than $1/T_p$, and the range resolution becomes deteriorate. As a result, the high speed of targets affects the range resolution of scatterers.

2) The influence of high speed on echo phases

In (5), the first and the second phases are all independent of the velocity v, which have no effect on the range compression result of the scatterer. Compare with (6), the third phase of (5) includes an additional speed-dependent first-order phase of fast time $-4\pi(\frac{v}{\lambda}-2\gamma v\frac{R_0(t_m)}{c^2})\hat{t}$, which will make range-compressed position of the scatterer shifted. And the fourth phase of (5) is the speed-dependent second-order phase of fast time, which will make the main lobe of the range-compressed result of the scatterer broaden.

In order to further analysis the influence of high speed on echo phases, we calculate the instantaneous frequency of (5) and (6) along the fast time-domain, respectively, and can obtain

$$f_h = -2\gamma\frac{R_0(t_m)-R_{\text{ref}}}{c} + \left(4\gamma v\frac{R_0(t_m)}{c^2}-2\frac{v}{\lambda}\right)+4\frac{v}{c}\gamma\left(\frac{v}{c}-1\right)\hat{t} \tag{8}$$

$$f_s = -2\gamma\frac{R_0(t_m)-R_{\text{ref}}}{c}. \tag{9}$$

By comparing (8) and (9), we can know that f_s is a constant. Thus, after taking the Fourier transform of (6) along the fast time-domain directly, the well-focused range-compressed result can be obtained. While f_h is an LFM frequency and it has a constant term $4\gamma v\frac{R_0(t_m)}{c^2}-2\frac{v}{\lambda}$ more than f_s. After taking the Fourier transform of (5) along the fast time-domain, the range-compressed result will be shifted and broadened.

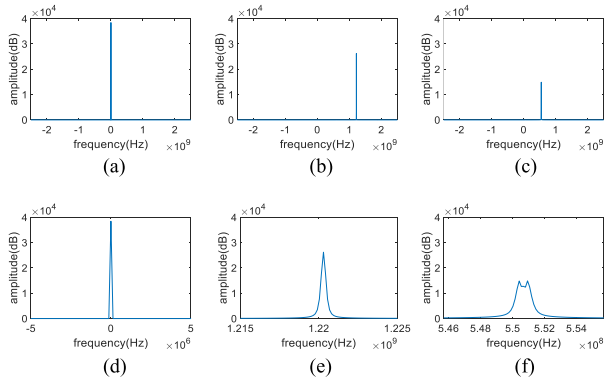

Fig. 1. Range-compressed results and its partial enlargement. The range-compressed results when (a) $v=0$ m/s ; (b) $v=2000$ m/s; (c) $v=5000$ m/s and (d), (e), (f) are the partial enlargement of (a), (b), (c), respectively.

In this article, the frequency $(4\gamma v\frac{R_0(t_m)}{c^2}-2\frac{v}{\lambda})+4\frac{v}{c}\gamma(\frac{v}{c}-1)\hat{t}$ in (8) is called the inner-pulse doppler frequency. The compensation algorithm for the inner-pulse doppler frequency will be given later.

Assume that a single scatterer moves at a uniform speed relative to ladar, the range-compressed results of this scatterer at different radial velocities are given below.

Set $T_p=7\ \mu$s, $\rho_r=0.94$ cm, $R_{\text{ref}}=100$ km, and $R_0(t_m)=R_{\text{ref}}$. Fig. 1(a), (b), and (c) are the range-compressed results of single scatterer when $v=0$m/s, $v=2000$m/s, and $v=5000$ m/s, respectively. Fig. 1(d), (e), and (f) are the partial enlargement of Fig. 1(a), (b), and (c), respectively.

From Fig. 1, we can see that the radial velocity of the scatterer relative to the radar will make the range-compressed position shifted and the main lobe of the range-compressed result broaden, which verify the conclusion that the influence of high speed on echo phases.

III. Inner-Pulse Doppler Compensation and Imaging Algorithm

According to the above analysis, we can know that the impact of the high speed on range-compressed mainly includes two aspects as follows:

1) The first-order phase introduced by radial velocity shifts the range-compressed position of the scatterer.
2) The second-order phase introduced by radial velocity broadens the main lobe of the range-compressed result of the scatterer.

Therefore, the first-order and the second-order phases of the echo caused by the high speed need to be compensated.

A. Inner-Pulse Doppler Compensation

1) Radial Velocity Estimation: Since the first-order phase and second-order phase are all related to the radial velocity v, the radial velocity v must be estimated before the phase compensation.

At present, the radial velocity estimation methods based on ISAL echo data mainly include: 1) the methods based on Doppler frequency rate, such as map drift [13], Radon—Wigner method

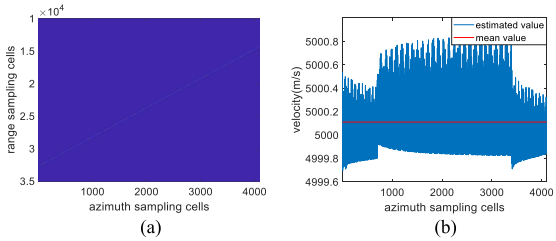

Fig. 2. (a) Range compression result of echo. (b) Estimated value of velocity.

[22], etc.; 2) the methods based on pulse frequency rate along the range direction, such as Chirp–Fourier [23], FrFT [15], [24], etc.; and 3) the method based on the offset of adjacent pulse envelopes [25].

In the above velocity estimation methods, method 1 and method 2 first estimate the frequency rate of the echo along the azimuth and range direction, respectively, and then use the frequency rate to calculate the radial velocity. These two methods have a high accuracy of velocity estimation, but they also require a large amount of computation. In contrast, the method 3 based on the offset of adjacent pulse envelopes requires a small amount of computation. Although the velocity estimation accuracy obtained by the method 3 is not high, it can meet the accuracy requirement for the high-speed motion compensation proposed in this article according to the analysis in Section III-A2 below. Therefore, we estimate the radial velocity by cross-correlation method of adjacent pulse envelopes in this article. The steps of the radial velocity estimation are as follows:

1) Calculate the cross-correlation function of adjacent pulses $\rho(m)$ ($m = 1 : M-1$, M is the number of accumulated pulses).
2) Search for the location of the maximum value of $\rho(m)$ and calculate the range units offset $\mathrm{Num}(m)$ between the adjacent pulses.
3) Calculate the radial velocity $v(m)$ between the adjacent pulses based on $\mathrm{Num}(m)$, minimum range resolution unit Δr and PRF (pulse repetition frequency), where $\Delta r = Fs/nrn \cdot c/(2\gamma)$ and Fs is sampling frequency. The specific expression of the estimated velocity is

$$v(m) = \mathrm{Num}(m) * \Delta r * \mathrm{PRF}. \tag{10}$$

4) Take the average value of $v(m)$ as the radial velocity estimation value $\widehat{v}$.

Assume that a scatterer moves at a speed of 5000 m/s relative to ladar, the process of the radial velocity estimation is as follows:

After dechirp receiving and Fourier transformation along the fast time-domain, the range-compressed result of the scatterer is shown in Fig. 2(a), in which the range-compressed result is a diagonal line. First, calculate $\rho(m)$, the location of the maximum value of $\rho(m)$ is $\mathrm{Num}(m)$. Then, calculate the radial velocity $v(m)$ based on $\mathrm{Num}(m)$, Δr, and PRF, the curve of $v(m)$ and the mean value of $v(m)$ are shown in Fig. 2(b). According to Fig. 2(b), we can know that the mean value of $v(m)$ is 5000.1, so the radial velocity estimation value is $\widehat{v} = 5000.1$, which is close to the true value 5000. Based on the above process, we can know that the velocity estimation algorithm used in this article requires a small amount of computation. Meanwhile, the range units offset $\mathrm{Num}(m)$ between the adjacent pulses can be used for envelope alignment before ISAR imaging.

Next, we will compensate for the inner-pulse Doppler term and RVP term by using $\widehat{v}$.

2) Compensation of the First-Order Phase and the Second-Order Phase: When the target moves relative to ladar, the radial velocity of all scatterers on the target are considered to be same. So according to (5), the dechirp received signal of all scatterers have the same first-order phase $-4\pi\frac{v}{\lambda}\hat{t}$ and second-order phase $4\pi\frac{v}{c}\gamma(\frac{v}{c}-1)\hat{t}^2$, and the dechirp received signal of a high-speed moving target can be viewed as the sum of multiple LFM signals with the same chirp rate. Therefore, we can construct the first-order and the second-order compensation functions based on the radial velocity and compensate the dechirp received signal of all scatterers uniformly.

Assume that the estimated speed is equal to the true value, i.e., $\widehat{v} = v$, in order to obtain the well-focused range-compressed result of the scatterers, we first construct the second-order compensation function h_1 using v

$$h_1 = \exp\left(-j4\pi\frac{v}{c}\gamma\left(\frac{v}{c}-1\right)\hat{t}^2\right). \tag{11}$$

After multiplying (5) by (11), we can obtain

$$\begin{aligned} s_{d1} = s_d \cdot h_1 = \sigma A \cdot \mathrm{rect}&\left(\frac{\alpha\hat{t} - 2R_0(t_m)/c}{T_p}\right) \\ \cdot \exp&\left(-j4\pi\left(\frac{R_0(t_m) - R_{\mathrm{ref}}}{\lambda} - \frac{\gamma}{c^2}\left(R_0^2(t_m) - R_{\mathrm{ref}}^2\right)\right)\right) \\ \cdot \exp&\left(-j4\pi\left(\frac{\gamma}{c}\left(R_0(t_m) - R_{\mathrm{ref}}\right) + \frac{v}{\lambda} - 2\frac{\gamma}{c^2}R_0(t_m)\,v\right)\hat{t}\right). \end{aligned} \tag{12}$$

Then, to avoid the shift of the range-compressed position of the scatterers, we construct the first-order compensation function h_2

$$h_2 = \exp\left(j4\pi\frac{v}{\lambda}\hat{t}\right). \tag{13}$$

After multiplying (12) by (13), we can obtain

$$\begin{aligned} s_{d2} = s_{d1} \cdot h_2 = \sigma A \cdot \mathrm{rect}&\left(\frac{\alpha\hat{t} - 2R_0(t_m)/c}{T_p}\right) \\ \cdot \exp&\left(-j4\pi\left(\frac{R_0(t_m) - R_{\mathrm{ref}}}{\lambda} - \frac{\gamma}{c^2}\left(R_0^2(t_m) - R_{\mathrm{ref}}^2\right)\right)\right) \\ \cdot \exp&\left(-j4\pi\left(\frac{\gamma}{c}\left(R_0(t_m) - R_{\mathrm{ref}}\right) - 2\frac{\gamma}{c^2}R_0(t_m)\,v\right)\hat{t}\right). \end{aligned} \tag{14}$$

Taking the Fourier transform of (14) along the fast time $\hat{t}$, we can obtain

$$\begin{aligned} s_{d2}(f_r) = \sigma A \cdot \frac{T_p}{\alpha}\,\mathrm{sinc}&\left(\frac{T_p}{\alpha}\left(f_r + 2\frac{\gamma}{c}\left(\alpha R_0(t_m) - R_{\mathrm{ref}}\right)\right)\right) \\ \cdot \exp&\left(-j4\pi\left(\frac{R_0(t_m) - R_{\mathrm{ref}}}{\lambda} - \frac{\gamma}{c^2}\left(R_0^2(t_m) - R_{\mathrm{ref}}^2\right)\right)\right) \\ \cdot \exp&\left(-j\frac{4\pi}{\alpha}\cdot\frac{R_0(t_m)}{c}\cdot\left(f_r + 2\frac{\gamma}{c}\left(\alpha R_0(t_m) - R_{\mathrm{ref}}\right)\right)\right). \end{aligned} \tag{15}$$

According to (15), the range-compressed position of the scatterer is

$$f_r = -2\frac{\gamma}{c}\left(\alpha R_0\left(t_m\right) - R_{\text{ref}}\right). \tag{16}$$

Equation (16) shows that the range-compressed position of the scatterers is relative to α. Therefore, when performing range calibration for high-speed moving target, the influence of velocity needs to be considered.

It should be point out that to avoid the main lobe of the range-compressed result be broadened, we define the velocity estimation error Δv meet the following constraint during the second-order phase compensation:

$$\left|4\pi\frac{v+\Delta v}{c}\gamma\left(\frac{v+\Delta v}{c}-1\right)T_p^2 - 4\pi\frac{v}{c}\gamma\left(\frac{v}{c}-1\right)T_p^2\right| < \frac{\pi}{4}. \tag{17}$$

The solution of this constraint is

$$\Delta v > \frac{c-2v-\sqrt{(c-2v)^2 - c^2/(4B\cdot T_p)}}{2}$$

$$\Delta v < \frac{c-2v-\sqrt{(c-2v)^2 + c^2/(4B\cdot T_p)}}{2}. \tag{18}$$

This means that the velocity estimation error Δv is related to v and $B\cdot T_p$.

B. Azimuth Focusing

1) RVP Correction: Submitting (16) into (15), we can obtain

$$s_{d2}\left(f_r\right) = \sigma A\cdot\frac{T_p}{\alpha}\sin c\left(\frac{T_p}{\alpha}\left(f_r + 2\frac{\gamma}{c}\left(\alpha R_0\left(t_m\right) - R_{\text{ref}}\right)\right)\right)$$
$$\cdot\exp\left(-j4\pi\frac{R_0\left(t_m\right)-R_{\text{ref}}}{\lambda}\right)\exp\left(-j\pi\left(1-\frac{2}{\alpha^2}\right)\frac{f_r^2}{\gamma}\right)$$
$$\cdot\exp\left(j\varphi\right) \tag{19}$$

where the first exponential term is the Doppler term. The second exponential term is the RVP term. The third exponential term is the residual phase term, whose expression is

$$\varphi = -\frac{4\pi}{\alpha^2 c}f_r R_{\text{ref}} - \frac{4\pi}{c^2}\gamma\left[\left(2\alpha-\frac{2}{\alpha}\right)R_{\text{ref}}R_0\left(t_m\right) + \left(1-\alpha^2\right)R_0^2\left(t_m\right)\right]. \tag{20}$$

As shown in (20) that the first phase of φ is a constant phase, the second phase of φ is the first-order phase of $R_0(t_m)$, and the third phase of φ is the second-order phase of $R_0(t_m)$. In this article, we assume that α is close to 1 and $\varphi < \pi/2$, so that the residual phase φ can be ignored.

To eliminate the RVP term in (19), we construct an RVP compensation function h_3

$$h_3 = \exp\left(j\pi\left(1-\frac{2}{\alpha^2}\right)\frac{f_r^2}{\gamma}\right). \tag{21}$$

After multiplying (19) by (21), we can obtain the range-compressed signal after RVP correction

$$s_{d3}\left(f_r\right) = s_{d2}\left(f_r\right)\cdot h_3$$

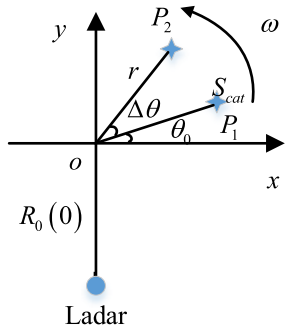

Fig. 3. ISAL turntable imaging geometry.

$$= \sigma A\frac{T_p}{\alpha}\cdot\sin c\left(\frac{T_p}{\alpha}\left(f_r + 2\frac{\gamma}{c}\left(\alpha R_0\left(t_m\right) - R_{\text{ref}}\right)\right)\right)$$
$$\cdot\exp\left(-j4\pi\frac{R_0\left(t_m\right)-R_{\text{ref}}}{\lambda} + j\varphi\right). \tag{22}$$

2) Translational Motion Compensation: ISAL imaging algorithms are all based on the turntable model. Therefore, before imaging, the translation component of relative motion between the target and ladar needs to be compensated.

Equation (22) is the range-compressed signal after RVP correction, in which $R_0(t_m)$ can be expressed as

$$R_0\left(t_m\right) = R^{\text{tra}}\left(t_m\right) + R^{\text{rot}}\left(t_m\right) \tag{23}$$

where $R^{\text{tra}}(t_m)$ represents the translation component of relative motion between the target and ladar.$R^{\text{rot}}(t_m)$ represents the rotation component of relative motion between the target and ladar.

$R^{\text{tra}}(t_m)$ can be expressed as

$$R^{\text{tra}}\left(t_m\right) = vt_m + 1/2\cdot a_r t_m^2 + \cdots \tag{24}$$

where v represents the radial velocity. a_r represents the acceleration.

Fig. 3 shows the ISAL turntable imaging geometry after the translational motion compensation. In Fig. 3, O is the center of the turntable and the turntable rotates around o. The distance from the ladar to o is $R_0(0)$. The y-axis is the line of sight of the ladar, and the x-axis is perpendicular to the y-axis. Initially, the scattering point S_{cat} is located at P_1. The distance from P_1 to o is r, and $r \ll R_0(0)$. The initial angle between P_1 and the x-axis is θ_0. Assume that the scattering point S_{cat} rotates from P_1 to P_2 with angular velocity ω, the rotation component of relative motion between the target and the ladar can be expressed as

$$R^{\text{rot}}\left(t_m\right) = R_0\left(0\right) + r\sin\left(\theta_0 + \omega t_m\right). \tag{25}$$

After the translational motion compensation of (22), we can obtain

$$s_{4d}\left(f_r\right) = \sigma A\cdot\frac{T_p}{\alpha}\sin c\left(\frac{T_p}{\alpha}\left(f_r + 2\frac{\gamma}{c}\left(\alpha R_{\text{rot}}\left(t_m\right) - R_{\text{ref}}\right)\right)\right)$$
$$\cdot\exp\left(-j4\pi\frac{R_{\text{rot}}\left(t_m\right)-R_{\text{ref}}}{\lambda} + \varphi - \varphi_0\right) \tag{26}$$

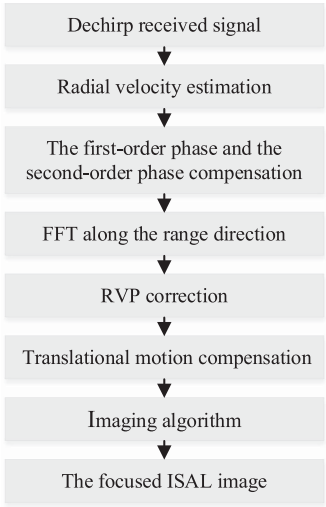

Fig. 4. Flow chart of the proposed algorithm.

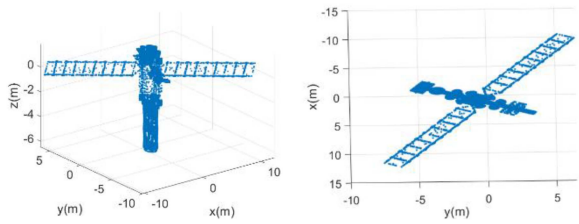

Fig. 5. 3-D models of the satellite target from different perspectives.

where φ_0 is the compensated constant phase during translation compensation.

Up to now, we can know that when the change of φ during the synthetic aperture time is less than $\pi/2$, (26) can be equivalent to the range-compressed result under the "stop-and-go" assumption, and then the traditional ISAL imaging algorithm can be used for high-resolution imaging of the target.

3) Imaging Algorithm: In traditional ISAL imaging, an appropriate imaging algorithm needs to be selected based on the size of the coherent accumulation angle of the target and whether the target is maneuvering.

If the coherent accumulation angle of the target is small, and the MTRC (migration though resolution cell) of the scatterers on the target not occur during the synthetic aperture time, we can use the RD (Range Doppler) algorithm for imaging. If the coherent accumulation angle of the target is large, and the MTRC of the scatterers on the target occur during the synthetic aperture time, the algorithms such as keystone and back projection can be used for imaging. And if the target exhibits strong maneuverability, the instantaneous imaging algorithms, such as short-time Fourier transform and Wigner Ville Distribution can be used for imaging.

To clearly describe the proposed algorithm, a flow chart is presented in Fig. 4.

As depicted in the flow chart, the first step of the proposed algorithm is to estimate the radial velocity and compensate for the first-order and second-order phases to eliminate the influence of inner-pulse Doppler caused by high-speed moving of targets. Then, the signal is Fourier transformed along the fast time-domain to obtain the range-compressed signal after inner-pulse Doppler compensation. Next, the RVP correction and the translational motion compensation are performed to the range-compressed signal. Finally, the focused ISAL image is obtained by selecting an appropriate imaging algorithm.

TABLE I
PARAMETERS USED IN THE SIMULATION

Parameter	Value	Parameter	Value
Wavelength	1064 nm	Rotation speed	2 mrad/s
Pulse width	7 us	Radial velocity	5000 m/s
Bandwidth	16 GHz	PRF	130 kHz
Fs	5 GHz	R0	100 km

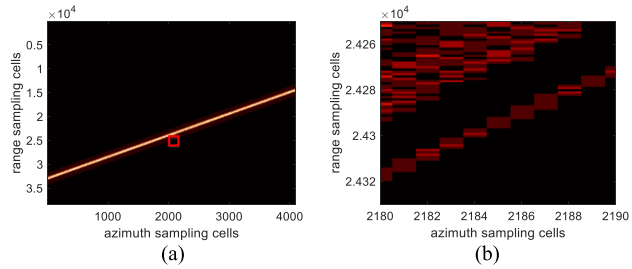

Fig. 6. (a) Range-compressed results of satellite target. (b) Partial enlargement of the red box in (a).

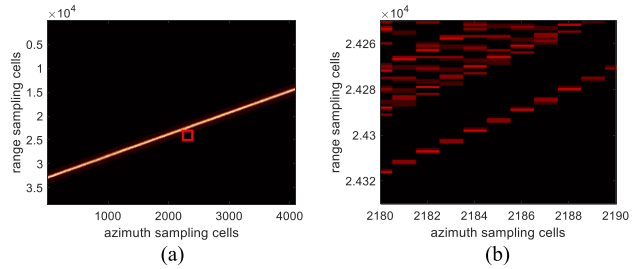

Fig. 7. (a) Range-compressed results of satellite target after the second-order phase compensation. (b) Partial enlargement of the red box in (a).

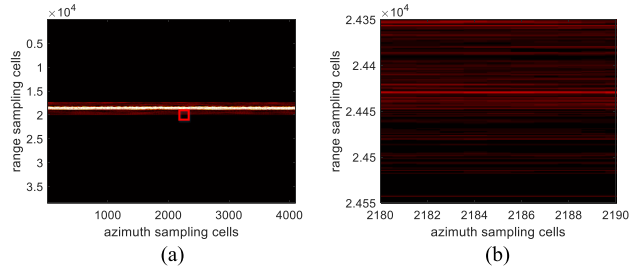

Fig. 8. (a) Range-compressed result of satellite target after the first-order phase compensation, the RVP correction, and the translational motion compensation. (b) Partial enlargement of the red box in (a).

IV. PROCESSING RESULTS OF THE SIMULATED DATA

Next, to verify the effectiveness of the proposed algorithm, different experiments are designed. Section IV-A shows the compensated results of the proposed algorithm. Section IV-B

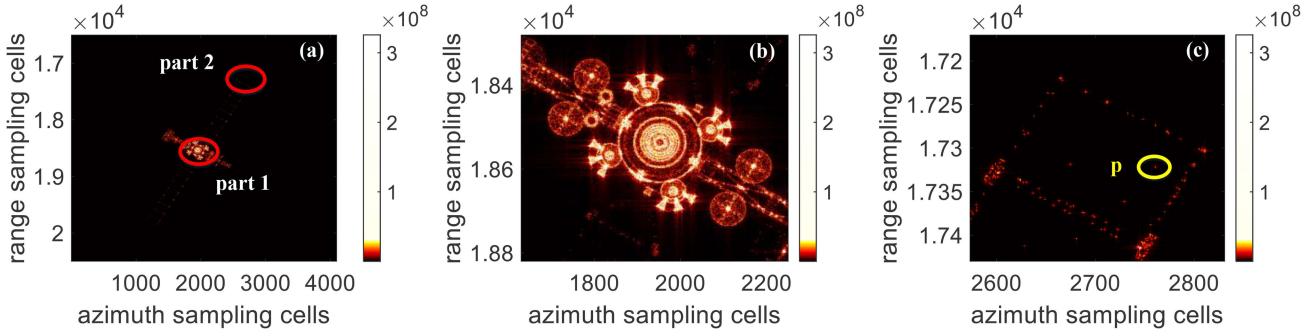

Fig. 9. (a) Imaging result of satellite targets by using the proposed algorithm. (b) Partial enlargement of part 1. (c) Partial enlargement of part 2.

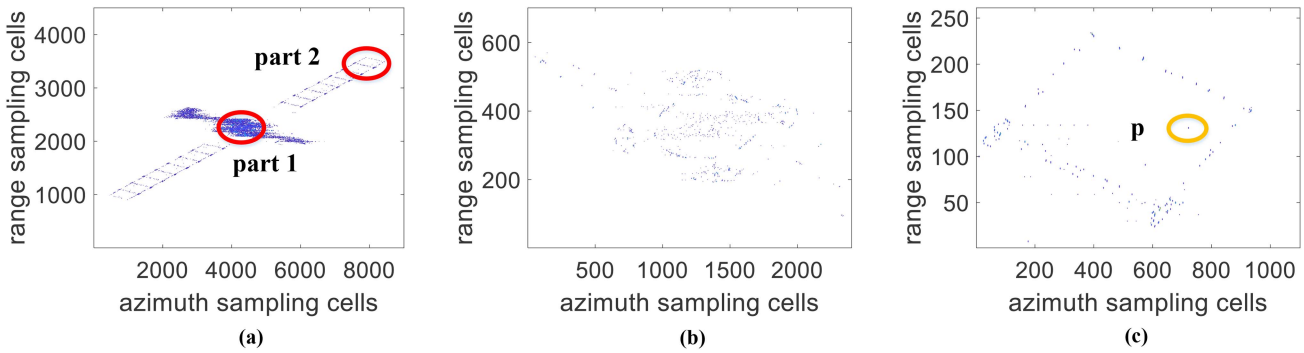

Fig. 10. (a) Imaging result of satellite target by using FC algorithm. (b) Partial enlargement of part 1. (c) Partial enlargement of part 2.

shows the performance of the proposed algorithm under different radial velocity estimated value. Section IV-C shows the performance of the proposed algorithm under different SNRs (signal–noise ratio).

A. Satellite Target Simulation Results

The simulated 3-D models of the satellite target from different perspectives are shown in Fig. 5, and the size of satellite is 22.77 m × 13.97 m × 8.3 m (x-axis × y-axis × z-axis).

Assume the ladar transmits an LFM signal with the parameters given in Table I. The coordinates of the satellite target are shown in Fig. 5, with the target rotating around the z-axis. The coordinate of the ladar is (R 0, 0, 0), where $R0$ represents the initial range between the satellite and the ladar. During the echo generation, $R0$ is set to 100 km, the satellite moves away from the ladar at the radial velocity of 5000 m/s along the x-axis and rotates around the z-axis at the rotation speed of 2 mrad/s.

Assume the coherent accumulation angle of the target is small, we choose RD algorithm as the imaging algorithm.

After dechirp receiving and Fourier transformation along the fast time-domain, the range-compressed result of the satellite target can be shown in Fig. 6. Fig. 6(b) is the partial enlargement of Fig. 6(a), which shows the main lobe of the range-compressed result is broadened. By compensating for the second-order phase of the echo, the range-compressed result with narrowed main lobe can be obtain as shown in Fig. 7. Fig. 7(b) is the partial enlargement of Fig. 7(a). By comparing Fig. 7(b) and (b), we can know that after the second-order phase compensation, the main lobe of the range-compressed result is narrowed.

Fig. 8(a) is the range-compressed result after first-order phase compensation, the RVP correction, and the translational motion compensation. Fig. 8(b) is the partial enlargement of Fig. 8(a), which shows that after the translational motion compensation, the range-compressed result changes from a diagonal line to a straight line.

Taking the Fourier transform of Fig. 8(a) along the azimuth direction, we can obtain the imaging result of the proposed algorithm shown in Fig. 9(a). Fig. 9(b) and (c) is the partial enlargement of part 1 and part 2 in Fig. 9(a), respectively. The scatterers in Fig. 9 are all well-focused.

The high-speed movement compensation algorithm in literature [21] is refers to as FC algorithm. Fig. 10(a) is the imaging result by using the FC algorithm, Fig. 10(b) and (c) is the partial enlargement of part 1 and part 2 in Fig. 10(a), respectively. Fig. 11(a) is the uncompensated imaging result. Fig. 11(b) and (c) is the partial enlargement of part 1 and part 2 in Fig. 11(a), respectively.

For comparison, Fig. 12(a), (b), and (c) shows the contour images of the point "P" in yellow circle in Figs. 11(c), 10(c), and 9(c), respectively. It can be seen that the point "P" in Fig. 12(a) is defocusing, and the point "P" in Fig. 12(b) and (c) exhibit better focus quality. This indicates that both the FC algorithm and the proposed algorithm all can eliminate the influence of high-speed movement of the target during ISAL imaging.

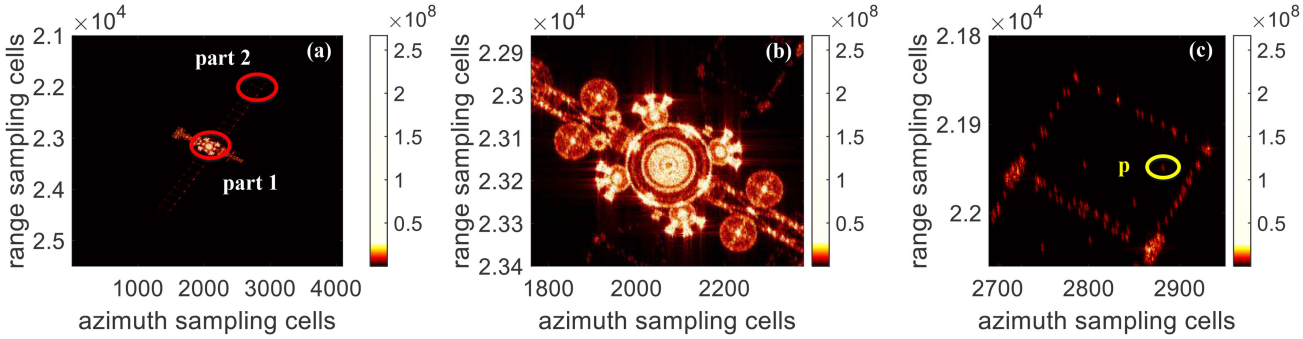

Fig. 11. (a) Uncompensated imaging result. (b) Partial enlargement of part 1. (c) Partial enlargement of part 2.

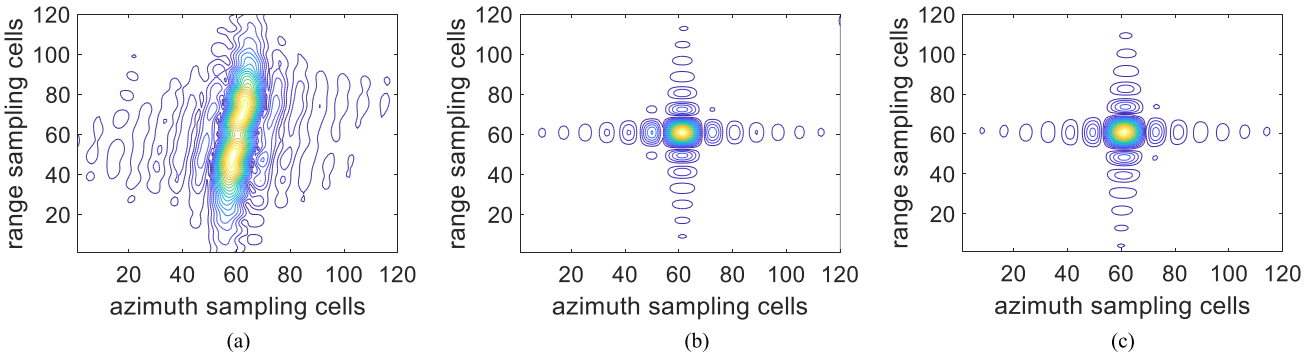

Fig. 12. Contour images of point "P" in yellow circle. (a) Uncompensated algorithm. (b) FC algorithm. (c) Proposed algorithm.

However, by comparing Figs. 9 and 10, we can know that some weak scatterers in Fig. 10 have been lost. This is caused by the nature of the CLEAN algorithm. In addition, the FC algorithm is computationally expensive, as it requires a search for the rotation angle that corresponds to the projection plane. In contrast, the proposed algorithm only needs to estimate the radial speed using a less computationally expensive speed estimation method. Therefore, compared to the FC algorithm, the proposed algorithm can retain more detailed information about the target while requiring less computation.

B. Performance of the Proposed Algorithm Under Different Radial Velocity Estimated Value

Based on the above analysis, we know that in order to avoid the main lobe of the range-compressed result broadened, the velocity estimation error Δv needs to meet the constraint of (17), in which the threshold value of the secondary phase compensation error is $\pi/4$. Submitting the parameters in Table I into (18), we can know that the corresponding range value of Δv is 166. If the threshold values of the secondary phase compensation error are $\pi/2$ and π, the corresponding value of Δv are 334 and 670 m/s, respectively.

We set the range of estimated radial velocity values v to be 4300–5700 m/s, with a step size of 2 m/s. Fig. 13 presents the entropy curve of the satellite imaging results under different v. In Fig. 13, the corresponding image entropy values at $\Delta v = 0$, 166, 334, and 670 m/s are marked. From Fig. 13, we can know that as Δv increases, the image entropy value becomes larger.

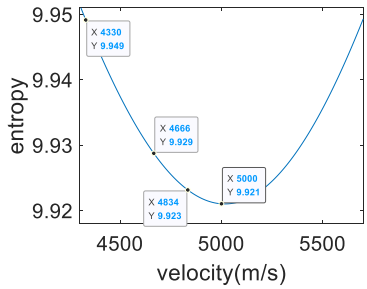

Fig. 13. Entropy curve of imaging results of the proposed algorithm under different radial velocity estimated value.

To further analyze the threshold of Δv, Fig. 14(a), (b), (c), and (d) shows the contour images of the point "P" in satellite target when $\Delta v = 0$, 166, 334, and 670 m/s, respectively. In which, Fig. 14(a) and (b) is well-focused, while Fig. 14(c) and (d) appears adhesions. This phenomenon indicates that when the threshold value of the secondary phase compensation error smaller than $\pi/4$, its effect on imaging can be ignored. Thus, the constraint of Δv derived in (17) and (18) is correct.

C. Performance of the Proposed Algorithm Under Different SNRs

To verify the performance of the proposed algorithm under different SNRs, the white Gaussian noise is added to the echo to generate different SNRs echo date.

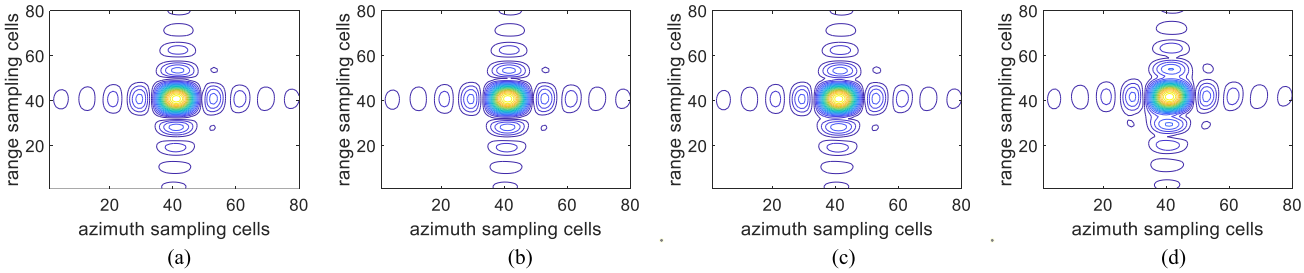

Fig. 14. Contour images of point "P" in satellite target, when (a) $\Delta v = 0$ m/s; (b) $\Delta v = 83$ m/s; (c)$\Delta v = 167$ m/s; and (d)$\Delta v = 334$ m/s.

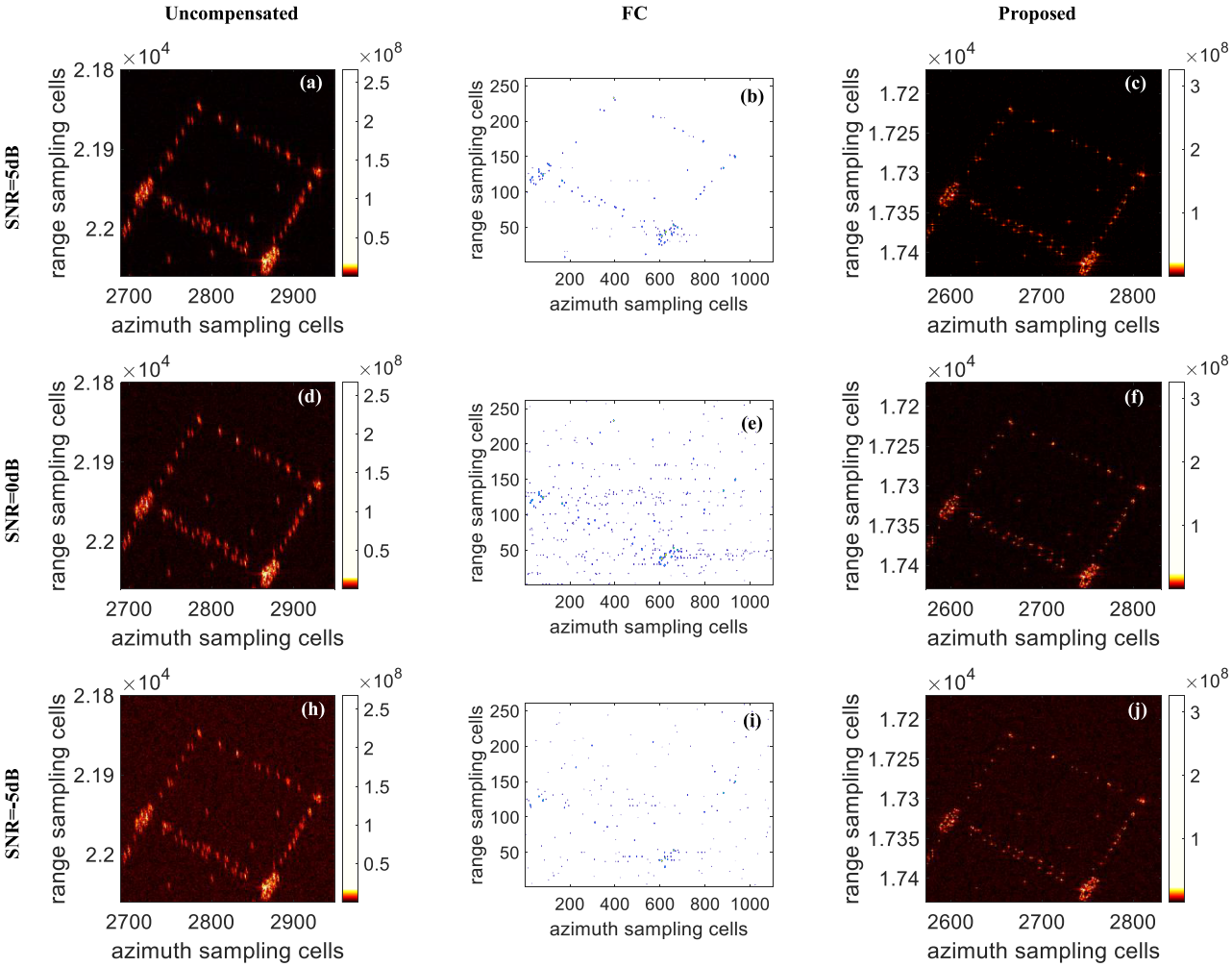

Fig. 15. Local imaging results of satellite solar panel obtained by different algorithm under different SNRs. (a), (d), (h) Uncompensated algorithm when SNR=5dB, 0dB and −5dB; (b), (e), (i) FC algorithm when SNR=5dB, 0dB and −5dB; (c), (f), (j) Proposed algorithm when SNR=5dB, 0dB and −5dB.

Fig. 15 shows the local imaging results of the satellite solar panel obtained by different algorithm when the SNR is 5, 0, and −5 dB, respectively. The velocities used for the phase compensation are all estimated by the number of sampling units offset of adjacent pulses.

The images obtained by the uncompensated algorithm are shown in the first column in Fig. 15, in which the scatterers are all defocused. The images obtained by the FC algorithm are given in the second column in Fig. 15, in which the number of scatterers reduces with the SNR decreases. When the SNR is 0 dB, the outline of the satellite solar panel can no longer be seen. The images obtained by the proposed algorithm are given in the third column in Fig. 15, in which the scatterers are all well-focused.

Table II presents the entropy values of the images shown in Fig. 15, in which the entropy value of the images obtained by the FC algorithm is smallest. This is because that the number of scatterers obtained by the FC algorithm reduces with the SNR decreases, but when the SNR is −5 dB, the outline of satellite solar panel can no longer be seen. Compared with the

TABLE II
ENTROPY OF THE IMAGING RESULTS

SNR value	5dB	0 dB	−5 dB
Uncompensated	12.8362	15.0828	17.0474
FC algorithm	7.7139	8.1306	9.0943
The proposed algorithm	12.5211	14.8756	16.9485

uncompensated algorithm, the images obtained by the proposed algorithm have smaller image entropy. This means that the proposed algorithm has good noise robustness.

V. DISCUSSION

Since ISAL is sensitive to the motion, the high-speed motion of the satellites will make the range-compressed result of scatterers shifted and broadened. To solve this problem, an ISAL imaging algorithm for spaceborne high-speed moving targets based on the inner-pulse Doppler compensation and RVP correction is proposed in this article, which derives the signal model of high-speed moving targets accurately and compensates for the phase related to velocity along the range and azimuth direction.

According to the processing results in Section IV, we can know the following conditions:

1) The proposed inner-pulse Doppler compensation method based on the velocity estimation is valid, which can suppress the main lobe broadening along the range direction.
2) During the inner-pulse Doppler compensation, the constraint condition of the velocity estimate error is derived. If the threshold value of the secondary phase compensation error is smaller than $\pi/4$, the velocity estimation error can be ignored.
3) When the SNR is -5 dB, all scatterers on the satellite are all well-focused, which means that the proposed algorithm has good noise robustness.
4) The proposed algorithm requires a small amount of computation and will not lose detail information of target.

In the following research, we can further analyze the residual phase φ shown in (20), for example, we can analyze how large the velocity is, φ can no longer be ignored, and given the corresponding compensation algorithm.

VI. CONCLUSION

The large radial velocity between the ladar and the observed satellite will make the range-compressed result of scatterers shifted and broadened. Therefore, we proposed a spaceborne ISAL imaging algorithm for high-speed moving targets based on the inner-pulse Doppler compensation and RVP correction. In this article, we give the estimated method of the radial velocity and the constraint condition of the velocity estimation accuracy, and the exact functions of inner-pulse Doppler compensation and RVP correction. By formula deducing, we find that after the RVP correction and the translational motion compensation, the date can be equivalent to the range-compressed result under the "stop-and-go" assumption, and then the target can be imaged by the traditional ISAL imaging algorithm. Various simulation experiments have verified the effectiveness of the proposed algorithm.

REFERENCES

[1] UCS, "UCS satellite databas[EB/OL]," (2023-1-1)[2023-4-28]. [Online]. Available: https://www.ucsusa.org/resources/satellite-database
[2] N. Bobrinsky and L. Del Monte, "The space situational awareness program of the European space agency," *Cosmic Res.*, vol. 48, no. 5, pp. 392–398, 2010.
[3] W. Jun, Z. Shuaiqin, and G. Ye, "High-orbit satellite recognition method based on HRRP characteristics of extended range radar," *Aerosp. Shanghai*, vol. 37, no. 4, pp. 88–95, 2020.
[4] J. Wang, L. Du, Y. Li, G. Lyu, and B. Chen, "Attitude and size estimation of satellite targets based on ISAR image interpretation," *IEEE Trans. Geosci. Remote Sens.*, vol. 60, no. 12, Dec. 2022, Art. no. 5109015.
[5] J. Wang, Y. Li, M. Song, and M. Xing, "Joint estimation of absolute attitude and size for satellite targets based on multi-feature fusion of single ISAR image," *IEEE Trans. Geosci. Remote Sens.*, vol. 60, no. 3, Mar. 2022, Art. no. 5111720.
[6] G. Liang, *Study on Experiment and Algorithm of Synthetic Aperture Imaging Lidar*. Shaanxi, China: Xidian Univ., 2009.
[7] Y. Hongfei et al., "Varying amplitude vibration phase suppression algorithm in ISAL imaging," *Remote Sens.*, vol. 14, no. 5, 2022, Art. no. 1122.
[8] G. Liang et al., "A novel sidelobe-suppression algorithm for airborne synthetic aperture imaging ladar," *Opt. Laser Technol.*, vol. 111, pp. 714–719, 2019.
[9] G. Liang et al., "Sub-aperture phase error stitching for full aperture airborne SAL data processing method based on azimuth deramp," *Opt. Laser Technol.*, vol. 136, 2021, Art. no. 106708.
[10] R. Hang, W. Yanhong, and Y. Wei, "Echo signal characteristics of inverse synthetic aperture ladar," *Laser Infrared*, vol. 43, no. 4, pp. 385–390, 2013.
[11] J. Sheng, C. Fu, H. Wang, and Y. Liu, "High speed motion compensation for terahertz ISAR imaging," in *Proc. Int. Appl. Comput. Electromagn. Soc. Symp.*, 2017, pp. 1–2.
[12] F. Zhou et al., "A stepped frequency synthetic preprocessing (SFSP) algorithm for ISAR imaging in fast moving target echo model," *IET Radar Sonar Navigation*, vol. 8, no. 8, pp. 864–874, 2014.
[13] M. Xing, R. Wu, and Z. Bao, "High resolution ISAR imaging of high speed moving targets," *IEE Proc.: Radar, Sonar Navigation*, vol. 152, no. 2, pp. 58–67, 2005.
[14] C. He and Z. Daiying, "High speed motion compensation based on the range profile," in *Proc. IEEE Int. Conf. Signal Process., Commun. Comput.*, 2013, pp. 1–4.
[15] M. Cao et al., "High resolution range profile imaging of high speed moving targets based on fractional Fourier transform," in *Proc. MIPPR Autom. Target Recognit. Image Anal.; Multispectral Image Acquisition; Int. Soc. Opt. Photon.*, 2007, Art. no. 678654.
[16] S. Zhang, S. Sun, and W. Zhang, "High-resolution bistatic ISAR image formation for high-speed and complex motion targets," *IEEE J. Sel. Topics Appl. Earth Observ. Remote Sens.*, vol. 8, no. 7, pp. 3520–3531, Jul. 2015.
[17] F. Wang, D. Jiang, and H. Chen, "High range resolution profile construction exploiting modified fractional Fourier transformation," *Math. Problems Eng.*, vol. 2015, 2015, Art. no. 321878.
[18] W. Jiadong et al., "Noise robust high-speed motion compensation for ISAR imaging based on parametric minimum entropy optimization," *Remote Sens.*, vol. 14, no. 9, 2022, Art. no. 2178.
[19] Y. Liu et al., "A novel speed compensation method for ISAR imaging with low SNR," *Sensors*, vol. 15, pp. 18402–18415, 2015.
[20] Y. Wang, J. Kang, and Y. Jiang, "ISAR imaging of maneuvering target based on the local polynomial Wigner distribution and integrated high-order ambiguity function for cubic phase signal model," *IEEE J. Sel. Topics Appl. Earth Observ. Remote Sens.*, vol. 7, no. 7, pp. 2971–2991, Jul. 2014.
[21] R. Hang, W. Yanhong, and Y. Wei, "Inverse synthetic aperture ladar imaging algorithm for maneuvering target based on FRFT-CLEAN," *J. Electron. Inf. Technol.*, vol. 35, no. 7, pp. 1540–1546, 2013.
[22] C. Wen, L. Zenghui, and Y. Jian, "Velocity estimation and compensation in FMCW-ISAR based on the iterative radon-Wigner transform," *J. Tsinghua Univ.*, vol. 54, no. 4, pp. 464–468, 2014.
[23] L. Wenmao and C. Yingliu, "Novel algorithm of high-speed target ISAR imaging based on stretch method," *J. Syst. Simul.*, vol. 28, no. 4, pp. 851–858, 2016.

[24] T. Pengfei et al., "Parameter estimation of multi-component LFM signals using integrated quadratic phase function and fractional Fourier transform," *Sci. China Ser. F Inf. Sci.*, vol. 28, no. 7, pp. 926–931, 2012.
[25] Z. Huanying, Z. Shouhong, and L. Qiang, "ISAR imaging of high speed moving targets," *J. Electron. Inf. Technol.*, vol. 29, no. 8, pp. 1789–1793, 2007.

Hongfei Yin was born in Inner Mongolia Province, China, in 1993. She received the B.S. degree from the Inner Mongolia University of Technology, Hohhot, China, in 2016, and the Ph.D. degree from the Xidian University, Xi'an, China, in 2022.

She is currently a Postdoctor with the Hangzhou Institute of Technology, Xidian University. Her research interests include synthetic aperture ladar, and inverse synthetic aperture ladar imaging.

Yachao Li (Member, IEEE) was born in Jiangxi Province, China, in 1981. He received the M.S. and Ph.D. degrees from the Xidian University, Xi'an, China, in 2005 and 2008, respectively, both in electrical engineering.

He is currently a Professor with the Xidian University. His research interests include SAR/ISAR imaging, missile-borne SAR imaging, ground moving target indication, matching and orientation of SAR image, real-time signal processing based on FPGA and DSP technology, and distributed radar.

Liang Guo (Member, IEEE) was born in Henan, China, in 1983. He received the B.S. degree from the Xidian University, Xi'an, China, in 2005, and the Ph.D. degree in signal and information processing from the Xidian University, in 2009.

He is currently a Full Professor with the School of Optoelectronic engineering, Xidian University. His research interests include imaging of several synthetic aperture radar modes, synthetic aperture ladar, and real-time imaging.

Songyuan Li (Graduate Student Member) was born in Hebei Province, China, in 1997. He received the B.S. degree from the Xidian University, Xi'an, China, in 2019. He is currently working toward the Ph.D. degree in optical engineering with the School of Optoelectronic Engineering, Xidian University.

His research interests include radar signal processing, synthetic aperture radar imaging, and radar jamming and antijamming technology.

Xuan Wang (Graduate Student Member) was born in Shaanxi Province, China, in 1997. He received the B.S. degree from the Xidian University, Xi'an, China, in 2019. He is currently working toward the Ph.D. degree in optical engineering with the School of Optoelectronic Engineering, Xidian University.

His research interests include radar signal processing, synthetic aperture ladar, and inverse synthetic aperture ladar imaging.

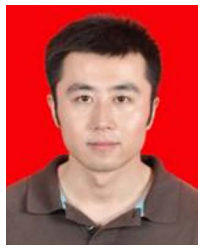

Liang Han was born in Shaanxi Province, China, in 1981. He received the Ph.D. degree in electronics science and technology from the Xi'an Jiaotong University, Xi'an, China, in 2011.

He is currently working with the School of Optoelectronic Engineering, Xidian University. His research interests include imaging of synthetic aperture radar in various modes.

Mengdao Xing (Fellow, IEEE) received the B.S. and Ph.D. degrees from the Xidian University, Xi'an, China, in 1997 and 2002, respectively.

He is currently a Professor with the National Laboratory of Radar Signal Processing, Xidian University. He holds the appointment of the Dean of the Academy of Advanced Interdisciplinary Research Department, Xidian University. He has authored or coauthored more than 200 refereed scientific journal articles. He also has authored or coauthored two books about synthetic aperture radar (SAR) signal processing. The total citation times of his research are greater than 10 000 (H-index 50). He was rated as the Most Cited Chinese Researcher by Elsevier. He has achieved more than 50 authorized China patents. His research has been supported by various funding programs, such as the National Science Fund for Distinguished Young Scholars. His research interests include SAR, SAR interferometry, inversed synthetic aperture radar, sparse signal processing, and microwave remote sensing.

Dr. Xing has held several special issues on IEEE GEOSCIENCE AND REMOTE SENSING MAGAZINE and IEEE JOURNAL OF SELECTED TOPICS IN APPLIED EARTH OBSERVATIONS AND REMOTE SENSING. He serves as an Associate Editor for radar remote sensing of the IEEE TRANSACTIONS ON GEOSCIENCE AND REMOTE SENSING and the Editor-in-Chief of *Sensors* (MDPI).